Annals of Glaciology



Paper

Cite this article: Woodard JB, Zoet LK, Iverson NR, Helanow C (2019). Linking bedrock discontinuities to glacial quarrying. *Annals of Glaciology* **60**(80), 66–72. https://doi.org/10.1017/aog.2019.36

Received: 28 June 2019
Revised: 21 October 2019
Accepted: 22 October 2019
First published online: 12 November 2019

Key words:
Basal ice; geomorphology; subglacial processes

Author for correspondence:
J. B. Woodard, E-mail: jacobwoodard88@gmail.com

© The Author(s) 2019. This is an Open Access article, distributed under the terms of the Creative Commons Attribution licence (http://creativecommons.org/licenses/by/4.0/), which permits unrestricted re-use, distribution, and reproduction in any medium, provided the original work is properly cited.

cambridge.org/aog

Linking bedrock discontinuities to glacial quarrying

J. B. Woodard[1], L. K. Zoet[1], N. R. Iverson[2] and C. Helanow[2]

[1]Department of Geoscience, University of Wisconsin-Madison, Madison, Wisconsin, USA and [2]Department of Geological and Atmospheric Sciences, Iowa State University of Science and Technology, Ames, Iowa, USA

Abstract

Quarrying and abrasion are the two principal processes responsible for glacial erosion of bedrock. The morphologies of glacier hard beds depend on the relative effectiveness of these two processes, as abrasion tends to smooth bedrock surfaces and quarrying tends to roughen them. Here we analyze concentrations of bedrock discontinuities in the Tsanfleuron forefield, Switzerland, to help determine the geologic conditions that favor glacial quarrying over abrasion. Aerial discontinuity concentrations are measured from scaled drone-based photos where fractures and bedding planes in the bedrock are manually mapped. A Tukey honest significant difference test indicates that aerial concentration of bed-normal bedrock discontinuities is not significantly different between quarried and non-quarried areas of the forefield. Thus, an alternative explanation is needed to account for the spatial variability of quarried areas. To investigate the role that bed-parallel discontinuities might play in quarrying, we use a finite element model to simulate bed-normal fracture propagation within a stepped bed with different step heights. Results indicate that higher steps (larger spacing of bed-parallel discontinuities) propagate bed-normal fractures more readily than smaller steps. Thus, the spacing of bed-parallel discontinuities could exert strong control on quarrying by determining the rate that blocks can be loosened from the host rock.

Introduction

Temperate glaciers are highly effective erosional agents resulting in denudation rates approaching 100 mm a^{-1} (Hallet and others, 1996). They profoundly affect landscape evolution and sedimentation rates (Hallet and others, 1996; Sternai and others, 2016; Ugelvig and others, 2016; Ugelvig and Egholm, 2018), with ancillary effects on processes as diverse as chemical weathering (e.g., Anderson, 2005) and volcanic eruptions (Sternai and others, 2016). The primary processes of glacial erosion are abrasion, the wearing away of underlying bedrock by debris entrained in basal ice, and quarrying (i.e., plucking), the fracturing and removal of bedrock blocks. Quarrying is commonly thought to be responsible for higher denudation rates than abrasion (Hildes and others, 2004; Loso and others, 2004; Riihimaki and others, 2005; Zoet and others, 2013). Quarrying rates are difficult to simulate due to the complex mechanisms involved and the difficulty of replicating quarrying in the laboratory. However, initial studies noted that quarrying can generally be divided into three phases (Röthlisberger and Iken, 1981; Iverson, 1991). A block must first become isolated from the surrounding bedrock through growth of fractures and their coalescence with preexisting discontinuities. Second, the isolated block must be extracted from its initial location. Finally, the extracted block must be entrained in the ice, thereby completing the erosion process.

Previous studies indicate that quarrying depends on the formation of subglacial cavities that concentrate stresses sufficiently to propagate factures subcritically in the bed (Iverson, 1991, 2012; Hallet, 1996; Cohen and others, 2006; Anderson, 2014). Subglacial cavities reduce the contact area between the ice and bed, thereby increasing normal stress on areas of ice-bed contact and the deviatoric stresses within the bedrock that lead to fracture propagation. Still, the additional normal stress is often insufficient to critically fracture competent rock layers, so slower subcritical fracture growth has been invoked to allow fracture propagation at stresses below the critical rock strength (Atkinson, 1987; Hallet, 1996). Subcritical crack growth results from weakening of the mineral bonds at crack tips via water, reducing the stresses necessary for fracture growth (Atkinson, 1987, 2008).

Although subcritical crack propagation induced by ice loading provides a convenient mechanism for quarrying, fracture patterns expected for glacier-induced subcritical cracks have not consistently been observed in the field. Glacier loading would induce fractures that propagate parallel to the maximum principal stress (σ_1) (perpendicular to the bedrock surface) and laterally extend perpendicular to the ice flow direction (Iverson, 1991). However, Hooyer and others (2012) showed that the strikes of quarried surfaces were independent of sliding direction and were dictated primarily by preexisting discontinuities in the bedrock that were exploited by sliding ice. Thus, cracks likely propagate due to ice loading but exploit pre-existing discontinuities in the rock, rather than initiating them (Iverson, 2012).

Past quarrying models estimate how basal stresses affect fracture growth but do so independent of the complex spatial variations of stress within the rock (Hallet, 1996; Iverson, 2012). To quantify fracture propagation velocities, linear-elastic fracture mechanics (LEFM)

are used (Walder and Hallet, 1985; Jaeger and others, 2007):

$$V = V_c\left[e^{\gamma\left(\frac{K_I^2}{K_c^2}-1\right)} - e^{\gamma\left(-\frac{8}{9}\right)}\right],\ K_c > K_I > 0.3\,K_C \qquad (1)$$

$V = 0,\ K_I \leq 0.3K_C$
$V = V_s,\ K_I \geq K_C$

$$K_I = \sigma_\perp^\infty (\pi c)^{\frac{1}{2}}, \qquad (2)$$

where V is the fracture propagation velocity, K_I is the stress intensity factor of a mode I (opening mode) fracture, K_C is rock fracture toughness (i.e., the critical stress intensity above which crack growth is critical), V_c and γ are the rock's growth-law parameters determined by plotting V vs K_I^2 on a log scale once K_c is known (Walder and Hallet, 1985), V_s is the critical fracture propagation velocity equal to the shear wave velocity in the rock, c is the crack length and $\sigma_\perp^\infty$ is the far-field tensile stress (oriented parallel to the top of the block). Table 1 defines all variables used herein. Importantly, an accurate estimation of K_I from Eqn 2 is possible only if stress is uniform (Atkinson, 1987; Hallet, 1996). If local stress variations are neglected in the estimation of K_I from Eqn 2, subglacial fractures can grow without bound under glacier loading (Eqns (1–2)). In most quarrying models, fracture propagation is the rate-limiting process. Thus, to obtain an accurate quarrying rate, a better understanding of how K_I varies in a subglacial environment is necessary.

Here we build on previous efforts to better characterize how geologic structure and subglacial stresses lead to quarrying. First, with photos from drone-base photogrammetry, we map the concentration of fractures in the forefield of Tsanfleuron Glacier, Switzerland, to determine if areas that are dominated by quarrying have a statistically greater concentration of aerially visible discontinuities than abrasion-dominated areas. No statistical correlation is found, suggesting another factor is dictating quarrying at Tsanfleuron. We explore the hypothesis that quarrying may be sensitive to the spacing of bed-parallel discontinuities generally not visible from air. Variation in the bed-parallel discontinuity spacing would likely alter the stress field in the bedrock and reduce the length fractures must travel to isolate a block, causing some areas to be quarried more readily than others. To test this hypothesis, we study fracture propagation dynamics on a subglacial stepped bed by using the COMSOL Multiphysics software to create a finite element model (FEM) to simulate stresses on a fracture propagating normal to the bed. These results provide insight into the bedrock and glacier conditions necessary for quarrying.

Setting

Tsanfleuron Glacier is located in the Rhone Valley of western Switzerland and overrides a 100–120 m thick Cretaceous limestone. In 2000, Tsanfleuron had a surface area of ~4 km^2 and an elevation ranging from 2420–2850 m a.s.l. (Hubbard and others, 2000). The exposed bedrock inside the Little Ice Age (LIA) moraine is largely debris free and consists of the Schrattenkalk (German) or Urgonian (French) Limestone (Gremaud and others, 2009; Bover-Arnal and others, 2011). The limestone of the forefield is folded into an anticline with an axial plunge of ~7° to the ENE that causes dips in the forefield to reach 25° to the SE (Gremaud and others, 2009). Our study sites consist of two ~0.5 km^2 areas of the exposed forefield within the Schrattenkalk Limestone, one near the ice margin and the other near the LIA moraine (Fig. 1). The mean ice-flow direction for both study sites was ~90° (i.e. due east) based on striation orientations measured in the field.

Table 1. Variables used in paper with values prescribed in the results

Parameter	Symbol (units)	Value (if constant)
Fracture propagation velocity	V (m s^{-1})	–
Growth-law parameter	V_c (m s^{-1})	–
Growth-law parameter	γ	–
Stress intensity factor	K_I (MPa m$^{1/2}$)	–
Fracture toughness	K_c (MPa m$^{1/2}$)	1.74
Critical fracture velocity	V_s (m s^{-1})	–
Far field tensile stress	$\sigma_\perp^\infty$ (Pa)	–
Crack length	c (m)	–
J-Integral	J (J m^{-2})	–
Strain energy density	W (J m^{-3})	–
Contour path	Γ	–
Crack stress component	σ_{ij} (Pa)	–
Crack displacement component	u_{ij} (m)	–
Crack normal vector component	n_i	–
Infinitesimal strain tensor	ε_{ij} (Pa)	–
Contour path arc length	s (m)	–
Young's modulus	E (Pa)	60×10^9
Normal stress	σ_n (MPa)	–

Methods

Discontinuity concentration

Aerial discontinuity concentrations within the forefield were determined using scaled photos to manually map discontinuities in the bedrock. Discontinuities were defined as any mappable break in the rock mass and consist of bedding planes, fractures or faults. Photos were collected from an unmanned aerial vehicle (UAV) that was fitted with a one-inch, 20-megapixel CMOS camera and F2.8 wide-angle lens with a 9 mm focal length, and was flown at an altitude of ~50 m above the rock surface. The UAV was capable of adjusting its flight altitude to maintain a uniform distance from the ground while collecting photos oriented perpendicular to the ground-surface. Digital elevation models (DEM) produced from the photos (via structure-from-motion) were used to scale the photos. DEMs were scaled by placing ground control points throughout the forefield with their positions precisely measured using an APS-3 RTK GPS system (0.01 m + 1 ppm), resulting in a DEM total error of ~ 0.1 m. The spatial resolution of each photo was determined by using six points common to the photo and DEM and then calculating the average of the 15 distance combinations between the points. Scaled photos and DEMs were produced for two sections of the forefield, an ice-proximal and an ice-distal section (Fig. 1). Root mean square (RMS)-roughness of the ice-proximal section of the forefield was substantially higher (8.5 m) than the ice-distal section (2.9 m), indicating a higher degree of quarrying in the ice-proximal section than in the ice-distal section (see Appendix A). Specific photos of rocks were selected that were clear of debris, showed clear quarrying surfaces (for quarried zones) or a lack of quarried surfaces (abraded zones), and best represented the fracture patterns of the area (Fig. 1). To assure only inherent discontinuities in the bedrock were included in our analysis, quarried surfaces were not mapped. Rather, fracture concentrations for the quarried zones were measured on unquarried rock immediately adjacent to the quarried zone, and aerial fracture concentrations were assumed similar between the quarried and immediately adjacent surfaces.

Discontinuities were manually mapped and analyzed using the methodology and code of Crompton and others (2018). A sampling window that captures the general trends of the whole photo was divided into expanded subsections to allow more detailed mapping of the photo area. Metrics used to determine the concentration of discontinuities were linear intensity (P_{10}), aerial intensity (P_{21}), aerial density (P_{20}), intersection density (I_{20}) and the ratio of minimum and maximum frequency (RMMF or max P_{10}/min P_{10}; Table 2). For a more detailed

https://doi.org/10.1017/aog.2019.36 Published online by Cambridge University Press

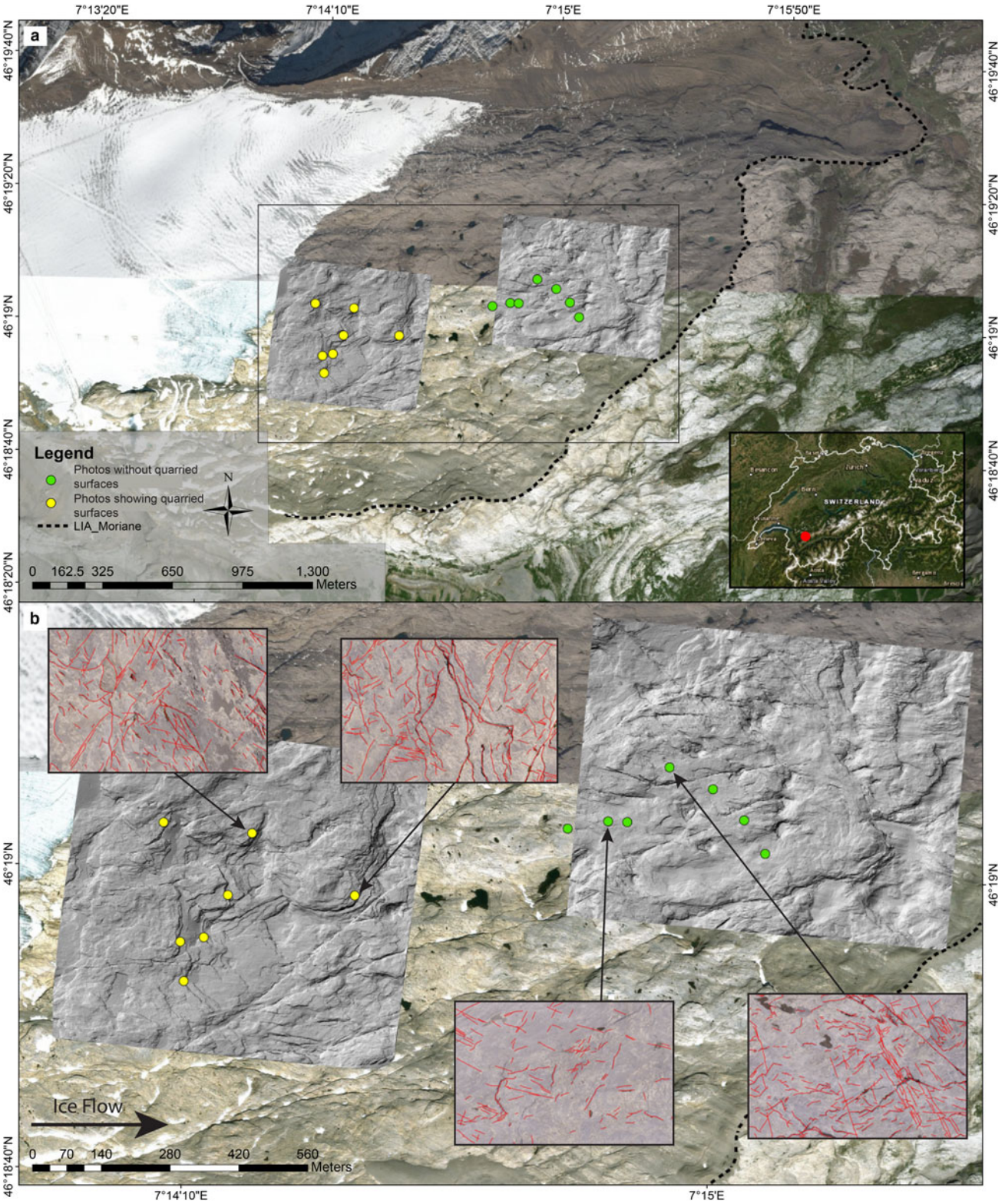


Fig. 1. DEMs with hillshading of the Tsanfleuron forefield overlain on 2012 and 2016 DigitalGlobe satellite imagery. Locations of photos with quarried surfaces (yellow dots) and without quarried surfaces (green dots), which were used for the fracture analysis, are also plotted. (a) Broad view of the forefield with the outer limit of the LIA moraine outlined with a black dashed line. The black box shows the location of (b). (b) Expanded portion of the forefield with inset photos that show examples of traced discontinuities in four photos.

explanation of these metrics see Crompton and others (2018). A pairwise Tukey honest significant difference (HSD) test ($\alpha = 0.05$), which is a conservative pairwise test that compares all possible pairs of means of the discontinuity metrics (Dowdy and others, 2011), was used to test the null hypothesis that the quarried and nonquarried zone metrics were statistically similar.

Fracture growth

To estimate the stresses on a bed-normal crack tip within a stepped bed and thereby model how a crack might propagate, we used the FEM package COMSOL. The COMSOL software package provides a platform with an array of predefined physics

https://doi.org/10.1017/aog.2019.36 Published online by Cambridge University Press

Table 2. Discontinuity metric symbology, name, description and *p*-values from the HSD test. All *p*-values indicate that there is no significant difference in discontinuity concentrations in quarried and nonquarried areas

Symbol (units)	Parameter	Description	*p*-value
P_{10} (m^{-1})	Linear intensity	Number of intersections between scanline and trace normalized by the total length of scanlines in window	0.97
P_{21} (m^{-1})	Aerial intensity	Sum of trace lengths normalized by window area	0.95
P_{20} (m^{-2})	Aerial density	Number of traces normalized by window area	0.37
I_{20} (m^{-2})	Intersection density	Number of trace intersections normalized by window area	0.93
RMMF	Ratio of max to min frequency	max P_{10}/min (P_{10})	0.34

interfaces that are capable of simulating fracture dynamics in the subglacial environment. Indirect estimates of how tensile stresses at the crack tip might change as it extends downward cannot be used with traditional LEFM because the expression for K_I (Eqn 2) is predicated on a uniform far-field tensile stress that does not change with crack length. Hence, this approach does not take into account either changes in tensile stress as cracks extend to greater depth or variations in rock geometry that might affect fracture growth. To overcome these limitations and to account for how stress singularities at the crack tip modify the local stress field and affect stress propagation, K_I was estimated using the *J*-integral (Rice, 1968) by determining the strain energy release rate for a growing crack.

The *J*-integral is a 2-D, path-independent line integral along contour Γ around the crack tip and is defined as

$$J = \int_{\Gamma} \left(W dy - n_i \sigma_{ij} \frac{\partial u}{\partial x} ds \right), \tag{3}$$

where σ_{ij} and u are the stress and displacement components, n_i is the normal vector component along Γ ($\sigma_{ij} n_i$ is often defined as the traction vector), ε_{ij} is the infinitesimal strain tensor, s is the arc length of Γ and W is the strain energy density (Rice, 1968; Atkinson, 1987)

$$W = \int_0^{e_{ij}} \sigma_{ij} \, d\varepsilon_{ij} \tag{4}$$

For a plane stress configuration in a linear elastic material the *J*-integral is related to K_I by

$$J = \frac{K_I^2}{E}, \tag{5}$$

where E is Young's modulus. Equations (3–5) allow the computation of K_I as a crack grows and affects local stresses acting on it. For a detailed explanation on the *J*-integral, see Rice (1968).

The *J*-integral was estimated in COMSOL after a FEM domain was constructed that replicated the stress regime of a stepped bed with subglacial cavities, partial ice-bed contact and a preexisting crack (Fig. 2). The geometry of the models consisted of a vertical step with heights of 1 or 2 m and a 5 m horizontal ledge on both sides of the step. An initial bed-normal crack 0.15 m long was considered 1 m from the step edge at the point of ice-bed reattachment. The crack was 1 mm wide at the surface and

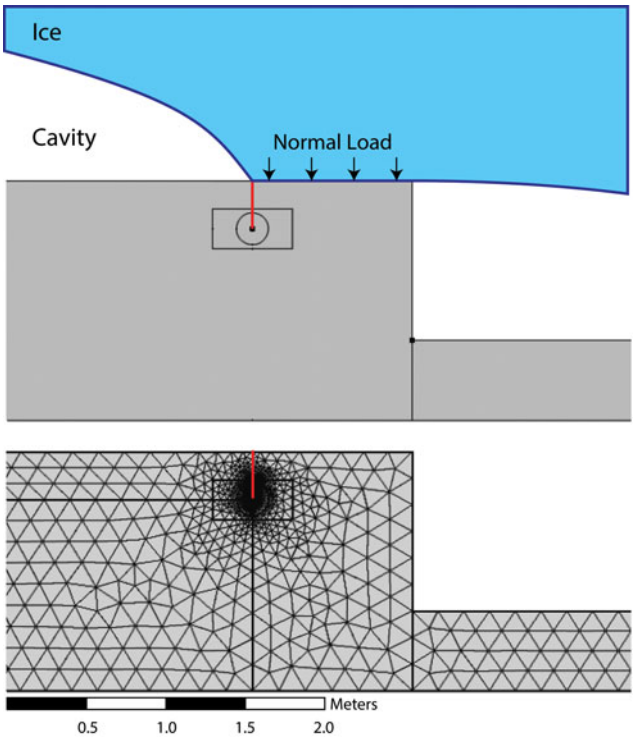


Fig. 2. FEM geometry and mesh used in the fracture-growth simulations. The red line shows the location of the fracture. The circle and rectangle around the crack tip are the paths of integration (Γ) used to calculate the *J*-integral. Water pressure in cavities is assumed to be zero to maximize the deviatoric stresses on the crack.

linearly tapered to single point, to mimic the geometry of an embedded crack. In order to maximize the deviatoric stresses that lead to fracture growth, we simulate a condition of low P_w in a large subglacial cavity by applying a normal stress (σ_n) to the area bounded by the crack and step edge, and no stresses on the rest of the ledge. The position of the crack relative to the ice-bed contact was chosen to produce the highest tensile stresses near the crack tip (Hetényi, 1960; Hallet, 1996). Rectangle and circle paths, Γ, were created around the crack tip as integration contours to determine the *J*-integral (Fig. 2). The crack length was incrementally extended by 1 and 2 cm for the 1 and 2 m step height simulations, respectively, until the crack extended to the depth of the ledge's base.

Results

Discontinuity concentration

Statistical comparison of the aerial discontinuity concentrations in the Tsanfleuron forefield indicates that the quarried zones are not statistically different from nonquarried zones. A total of 14 different zones of the forefield were analyzed, seven located in quarried areas and seven in nonquarried areas (Fig. 1). All *p*-values from the Tukey HSD test are greater than 0.3 (Table 2) indicating that aerially visible discontinuities alone are unlikely to have been the controlling factor in determining if an area was dominated by quarrying or abrasion.

Fracture growth

The FEM analysis reveals that stress intensities at the crack tip decline as the crack grows downward and that small variations in σ_n associated with changes in water pressure (e.g. Anderson, 2014) can cause highly variable fracture-growth dynamics. Figure 3 shows the Von Mises stress distribution on the stepped

https://doi.org/10.1017/aog.2019.36 Published online by Cambridge University Press

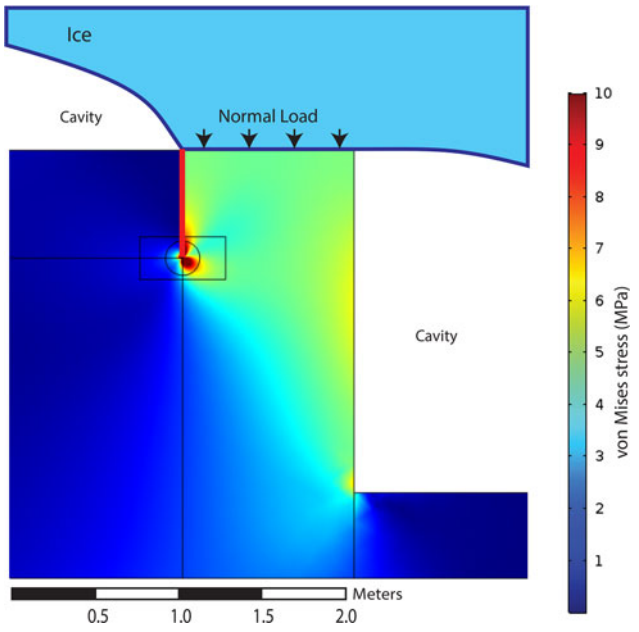


Fig. 3. Von Mises stress from an applied normal load on a step. The stress range was limited to 10 MPa to illustrate the distribution of stresses throughout the bed due to the stress singularity at the crack tip. The red line shows the location of the fracture. The circle and square around the crack tip are the paths of integration (Γ) used to calculate the *J*-integral.

bed with an applied normal load of 5 MPa and illustrates that the highest stress is at the crack tip (note that stress range was limited to 10 MPa due to the stress singularity). Von Mises stress is a theoretical measure used to estimate the stresses necessary for a material to yield (see Jaeger and others, 2007). Figure 4 shows the stress intensity factors (or $(J \cdot E)^{1/2}$) from the FEM for a 1 and 2 m step height with σ_n on the block varying from 1 to 5 MPa (solid lines). The fracture toughness (K_c, dotted line) and the threshold for subcritical crack growth ($K_c/3$, dash-dotted line) for Balmholtz limestone (Atkinson, 1987) are plotted for reference. Typical values for fracture toughness of rock range from 0.3 to 3.7 (Atkinson, 1987). The $K_I$values from Eqn 2 with $\sigma_\perp^\infty = 2\sigma_n/3$ as used by Hallet (1996) are also plotted (dashed lines) for reference. For the 1 m step simulation, the maximum stress intensity is located near the ice-bed contact, whereas in the 2 m step simulation stress peaks at ~0.4 m depth and then, importantly, begins to decrease with depth. In all simulations, higher σ_n values at the surface increase the overall K_I, but the effect is amplified for the larger step height (Fig. 4). As the crack tip approaches the level of the base of the step, K_I values in both simulations converge to approximately the same value, suggesting the stress regime is the same at that point regardless of step height. The stresses at the crack tip approach the limestone's critical level if σ_n >3 MPa and >2 MPa for the 1 and 2 m step height simulations, respectively. We calculate greater K_I values than did Hallet (1996) near the ice–bed interface, but at depth this monotonically increasing K_I values exceed the declining K_I values of this study (Fig. 4).

Discussion

If aerially visible fractures are not the controlling factor for quarrying at Tsanfleuron, perhaps the spacing of bed-parallel discontinuities, such as bedding planes, are more important for controlling quarrying. FEM results indicate that lower σ_n values are needed for bed-normal fracture propagation in the 2 m step simulation compared to the 1 m step simulation, and thus bed-normal fractures in thicker beds can propagate more readily under equal stress conditions (Fig. 4). For example, if we assume the normal stress acting on the bed is 3 MPa (blue line Fig. 4), the fracture in the 2 m step will fail critically ($V = V_s$) until $c \rightarrow$ 1.4 m, after which it will continue to propagate subcritically at a reduced velocity (Eqn 1). In contrast, the 1 m step will never critically fail but will stay in the subcritical regime in which velocities are much smaller than critical velocities. The reason for this variation with a step height is likely due to the buttressing effect of the lower step inhibiting crack growth below that depth, coupled with the potential for longer cracks in the 2 m step to focus more stress at the crack tip. The ledge of the lower step would reduce the tensile stress as the crack approaches the level of the base of the step, which explains why K_I values are similar at the base of the steps for both step

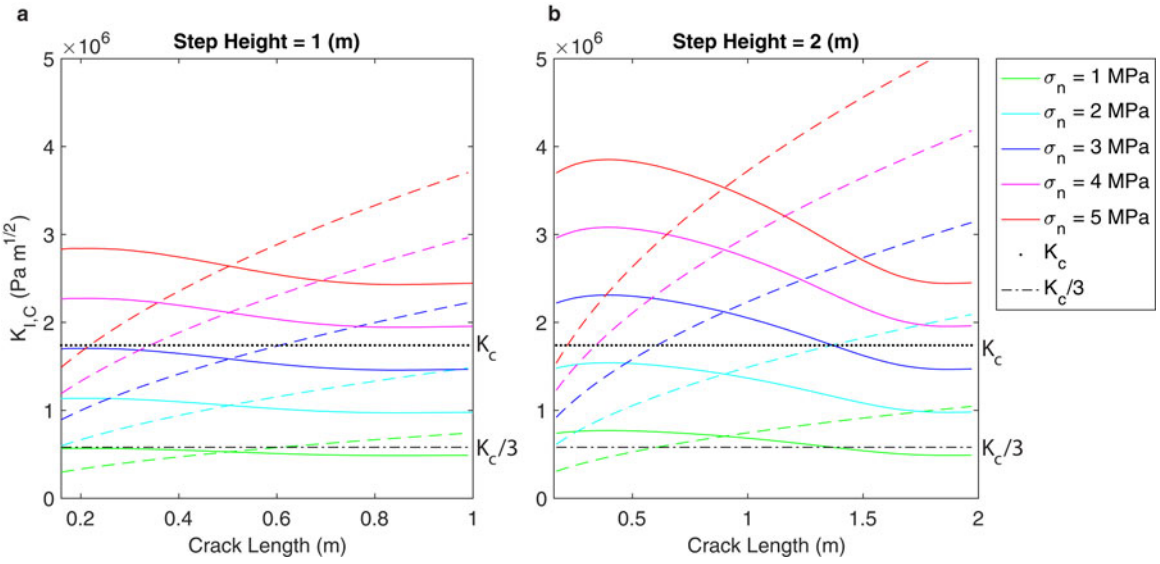


Fig. 4. Stress intensity (K_I) values for FEM simulations with step heights of 1 and 2 m. Solid lines show K_I values from the FEM simulations at variable applied normal stresses (σ_n) on the top of the block. Dashed lines are the values based on Eqn 2 and the correction factor 0.66 used by Hallet (1996) to convert applied normal stresses to far-field tensile stresses. The dotted line is the fracture toughness (K_c) value for Balmholtz limestone. The dot-dashed line is the threshold for subcritical crack growth ($K_c/3$).

https://doi.org/10.1017/aog.2019.36 Published online by Cambridge University Press

heights, while increased crack length would lead to increased K_I. Consequently, under equal loading conditions, thicker beds (larger steps) would facilitate fracture propagation and quarrying rates and could be a possible explanation for the observed spatial variability of quarried areas where fracture concentrations are statistically similar.

The traditional equations for determining K_I in LEFM are not suitable for the complex stress regimes associated with quarrying. As stated by Atkinson (1987), 'application to real rock mechanics problems of the concepts and theories [of crack initiation and propagation] will almost always require the use of the computer and a numerical method such as finite or boundary elements.' Figure 4 shows that K_I values determined from Eqn 2 will result in an increase in calculated stress at the tip of the crack as it grows that will lead to exaggerated fracture velocities (Eqn 1) and runaway crack growth. In contrast, FEM simulations of this study demonstrate that after an increase in K_I during initial crack growth, K_I values decrease, potentially halting growth of a fracture once it has extended sufficiently far from the bed surface, the exact opposite of the LEFM analysis. Precise estimates of K_I are necessary for determining the rates of quarrying, owing to the high sensitivity of V to K_I.

Inherent bedrock properties (i.e., discontinuity orientation, length and spacing etc.) play important roles in determining if rock will quarry (Hooyer and others, 2012). The K_c value of a rock dictates the depth to which a fracture could propagate for a given applied stress (Fig. 4). Assuming that crack growth rate limits the quarrying rate, lower K_c values increase fracture propagation rates and maximum penetration depths, accelerating quarrying, whereas high K_c values inhibit it. Pre-existing bed-parallel discontinuities are necessary for the extraction phase of quarrying, while preexisting bed-normally oriented fractures are required for bed-normal fracture propagation from ice-induced tensile stresses.

The FEM results suggest that the spatial variation in quarrying prominence observed at Tsanfleuron without an associated change in concentrations of aerial discontinuities could be due to a difference in the spacing of bed-parallel discontinuities. Under the conditions explored with the FEM, greater step heights (i.e., bed-parallel discontinuity spacing) would facilitate critical crack growth for much of the step height (see 3 MPa example in Fig. 4), allowing blocks to be isolated from the intact bedrock relatively quickly. In contrast, smaller step heights would cause bed-normal fractures to propagate subcritically or remain static (Eqns (1–2)), potentially preventing the fractures from reaching the bed-parallel discontinuities, or isolating the block, within the time frame of glacial coverage. It follows that if the ice-proximal region of the forefield has thicker bedding compared to the ice-distal region, thicker beds would enable accelerated fracture propagation and quarrying without a higher concentration of aerial discontinuities. This provides a plausible explanation for the increased degree of quarrying in the ice-proximal region of the forefield compared to the ice-distal region.

Conclusion

In the Tsanfleuron forefield, the concentration of aerial discontinuities is not statistically different in quarried and nonquarried areas. To explore why, we analyze how spacings and orientations of bedrock discontinuities oriented parallel to the bed might affect the quarrying process. FEM results show that taller steps lead to higher fracture propagation rates compared to smaller steps, hence the step size may be an important control on quarrying. These results suggest that fracture growth is facilitated by larger step sizes and exploits pre-existing discontinuities in the bedrock. Future work should explore with the FEM model how proximity of a fracture to the step edge will change the stress field at the crack tip, and consequently, propagation rates of bed-normal fractures. In addition, the development of an analytical or empirical equation for determining K_I based on the bed geometry would allow easier implementation of these results into erosion models.

Acknowledgements. We acknowledge funding support for this work was provided by the US National Science Foundation Division of Earth Sciences Program grant EAR166104 to NRI and LKZ. We thank B. Hallet and H. Sone for their helpful discussions. We also thank the reviewers for their valuable comments.

References

Anderson SP (2005) Glaciers show direct linkage between erosion rate and chemical weathering fluxes. *Geomorphology* **67**(1–2), 147–157. doi: 10.1016/J.GEOMORPH.2004.07.010.

Anderson RS (2014) Evolution of lumpy glacial landscapes. *Geology* **42**(8), 679–682. doi: 10.1130/G35537.1.

Atkinson BK (1987) *Fracture Mechanics of Rock*. Orlando, Florida: Academic Press.

Atkinson BK (2008) Subcritical crack growth in geological materials. *Journal of Geophysical Research: Solid Earth* **89**(B6), 4077–4114. doi: 10.1029/jb089ib06p04077.

Bover-Arnal T, Jaramillo-Vogel D, Showani A and Strasser A (2011) Late Eocene transgressive sedimentation in the western Swiss Alps: Records of autochthonous and quasi-autochthonous biofacies on a karstic rocky shore. *Palaeogeography, Palaeoclimatology, Palaeoecology* **312**(1–2), 24–39. doi: 10.1016/j.palaeo.2011.08.006.

Cohen D, Hooyer TS, Iverson NR, Thomason JF and Jackson M (2006) Role of transient water pressure in quarrying: a subglacial experiment using acoustic emissions. *Journal of Geophysical Research: Earth Surface* **111**(3), 1–13. doi: 10.1029/2005JF000439.

Cooley JW and Tukey JW (1965) An algorithm for the machine calculation of complex Fourier series. *Mathematics of Computation* **19**(90), 297–297. doi: 10.1090/S0025-5718-1965-0178586-1.

Crompton JW, Flowers GE and Stead D (2018) Bedrock fracture characteristics as a possible control on the distribution of surge-type glaciers. *Journal of Geophysical Research: Earth Surface* **123**(5), 853–873. doi: 10.1002/2017JF004505.

Dowdy S, Wearden S and Chilko D (2011) *Statistics for Research*, 3rd Edn. New York: John Wiley & Sons.

Gremaud V, Goldscheider N, Savoy L, Favre G and Masson H (2009) Geological structure, recharge processes and underground drainage of a glacierised karst aquifer system, Tsanfleuron-Sanetsch, Swiss Alps. *Hydrogeology Journal* **17**(8), 1833–1848. doi: 10.1007/s10040-009-0485-4.

Hallet B (1996) Glacial quarrying: a simple theoretical model. *Annals of Glaciology* **22**, 1–8.

Hallet B, Hunter L and Bogen J (1996) Rates of erosion and sediment evacuation by glaciers: a review of field data and their implications. *Global and Planetary Change* **12**, 213–235.

Hetényi M (1960) A method of solution for the elastic quarter-plane. *Journal of Applied Mechanics* **27**, 289–296

Hildes DHD, Clarke GKC, Flowers GE and Marshall SJ (2004) Subglacial erosion and englacial sediment transport modelled for North American ice sheets. *Quaternary Science Reviews* **23**(3–4), 409–430. doi: 10.1016/j.quascirev.2003.06.005.

Hooyer TS, Cohen D and Iverson NR (2012) Control of glacial quarrying by bedrock joints. *Geomorphology* **153–154**, 91–101. doi: 10.1016/j.geomorph.2012.02.012.

Hubbard B, Siegert MJ and McCarroll D (2000) Spectral roughness of glaciated bedrock geomorphic surfaces: implications for glacier sliding. *Journal of Geophysical Research: Solid Earth* **105**(B9), 21295–21303. doi: 10.1029/2000JB900162.

Iverson NR (1991) Potential effects of subglacial water pressure fluctuations on quarrying. *Journal of Glaciology* **37**(125), 27–36. doi: 10.1017/S0022143000042763.

Iverson NR (2012) A theory of glacial quarrying for landscape evolution models. *Geology* **40**(8), 679–682. doi: 10.1130/G33079.1.

Jacobs TDB, Junge T and Pastewka L (2017) Quantitative characterization of surface topography using spectral analysis. *Surface Topography: Metrology and Properties* **5**(1). doi: 10.1088/2051-672X/aa51f8.

Jaeger JC, Cook NGW and Zimmerman RW (2007) *Fundamentals of Rock Mechanics*, 4th Edn. Blackwell Publishing, Malden, MA

Loso MG, Anderson RS and Anderson SP (2004) Post–Little Ice Age record of coarse and fine clastic sedimentation in an Alaskan proglacial lake. *Geology* **32**(12), 1065. doi: 10.1130/G20839.1.

Perron JT, Kirchner JW and Dietrich WE (2008) Spectral signatures of characteristic spatial scales and nonfractal structure in landscapes. *Journal of Geophysical Research: Earth Surface* **113**(4), 1–14. doi: 10.1029/2007JF000866.

Press WH, Flannery BP, Teukolsky SA and Vetterling WT (1986) *Numerical Recipes*. New York, NY: Cambridge University Press.

Priestley MB (1981) *Spectral Analysis and Time Series*. New York: Academic Press.

Rice JR (1968) A path independent integral and the approximate analysis of strain concentration by notches and cracks. *Journal of Applied Mechanics* **35**(2), 379. doi: 10.1115/1.3601206.

Riihimaki CA and 9 others (2005) Sediment evacuation and glacial erosion rates at a small alpine glacier. *Journal of Geophysical Research* **110**, 3003. doi:10.1029/2004JF000189.

Röthlisberger H and Iken A (1981) Plucking as an effect of water-pressure variations at the glacier bed. *Annals of Glaciology* **2**, 57–62. doi: 10.3189/172756481794352144.

Sternai P, Caricchi L, Castelltort S and Champagnac JD (2016) Deglaciation and glacial erosion: a joint control on magma productivity by continental unloading. *Geophysical Research Letters* **43**(4), 1632–1641. doi:10.1002/2015GL067285.

Ugelvig SV and Egholm DL (2018) The influence of basal-ice debris on patterns and rates of glacial erosion. *Earth and Planetary Science Letters* **490**, 110–121. doi: 10.1016/j.epsl.2018.03.022.

Ugelvig S V, Egholm DL and Iverson NR (2016) Glacial landscape evolution by subglacial quarrying : a multiscale computational approach. *Journal of Geophysical Research: Earth Surface*, **121**, 1–27 (doi: 10.1002/2016JF003960)

Walder JS and Hallet B (1985) A theoretical model of the fracture of rock during freezing. *GSA Bulletin* **96**, 336–346. doi: 10.1130/0016-7606(1985)96<336.

Zoet LK and 6 others (2013) The effects of entrained debris on the basal sliding stability of a glacier. *Journal of Geophysical Research: Earth Surface* **118**(2), 656–666. doi:10.1002/jgrf.20052.

Appendix A

Roughness

To quantitatively distinguish quarried and abraded zones we measure the 2-D RMS roughness (R) values of the upper and lower sections of the forefield shown in Figure 1. Heavily quarried areas will have a higher Rvalue compared to abraded areas. R is calculated on the detrended forefield elevation data that have been oriented so the mean ice flow direction is across the x-axis, $z(x, y)$. The surface data consist of $N_x \times N_y$ measurements spaced at even intervals ($\Delta x,\ \Delta y$) by taking the integral of the window-normalized discrete power density spectrum (Press and others, 1986; Perron and others, 2008; Jacobs and others, 2017)

$$R = \sum_{m=0}^{N_x-1} \sum_{n=0}^{N_y-1} (P_{\mathrm{DFT}}(k_{m\Delta x}, k_{n\Delta y}))^{0.5} \tag{A1}$$

$$P_{\mathrm{DFT}}(k_{m\Delta x}, k_{n\Delta y}) = \left(N_x N_y \sum_{m=0}^{N_x-1} \sum_{n=0}^{N_y-1} W_h(m, n)^2 \right)^{-1} |Z(k_{m\Delta x}, k_{n\Delta y})|^2 \tag{A2}$$

$$Z(k_{m\Delta x}, k_{n\Delta y}) = \sum_{m=0}^{N_x-1} \sum_{n=0}^{N_y-1} (z \cdot W)(m\Delta x, n\Delta y) e^{-2\pi i \left(\frac{k_x m}{N_x} + \frac{k_y n}{N_y} \right)} \tag{A3}$$

where k_x and k_y are wavenumbers along the x and y axes of the topographic section, m and n are indices of the z array, W_{h} is the Hann window function and Z is the discrete 2D-fast Fourier transform (Cooley and Tukey, 1965). Note that $m\Delta x = x$ and $n\Delta y = y$. Window normalization of the detrended surface data is necessary because the Fourier transform assumes the input surface is periodic. Otherwise the resulting power spectrum becomes contaminated (Priestley, 1981; Press and others, 1986). The spectral roughness is equivalent to the variance, or integral divided by the area, of the detrended elevation data z. The RMS roughness of the upper section was 8.5 m, whereas the lower section had a value of 2.9 m, suggesting that the degree of quarrying is higher in the ice-proximal section of the forefield compared to the ice-distal section.

https://doi.org/10.1017/aog.2019.36 Published online by Cambridge University Press